International Journal of Pressure Vessels and Piping 128 (2015) 18–35

Contents lists available at ScienceDirect

International Journal of Pressure Vessels and Piping

journal homepage: www.elsevier.com/locate/ijpvp

Delamination effects on fracture behavior of a pipeline steel: A numerical investigation of 3-D crack front fields and constraint

C. Ruggieri [a, *], E. Hippert Jr. [b]

[a] Department of Naval Architecture and Ocean Engineering, University of São Paulo, São Paulo, SP 05508–900, Brazil
[b] Petrobras Development and Research Center (TMEC-CENPES), Rio de Janeiro, RJ, Brazil

ARTICLE INFO

Article history:
Received 1 December 2014
Received in revised form
16 January 2015
Accepted 16 January 2015
Available online 24 January 2015

Keywords:
Delamination cracking
Splitting
Fracture toughness
Constraint effects
API X70 steel

ABSTRACT

This work addresses a numerical investigation of the crack front fields and effects of crack-tip constraint in conventional fracture specimens with prescribed transverse delamination cracks. One purpose of this study is to conduct a systematic evaluation of delamination effects in side-grooved and plane-sided C(T) and clamped SE(T) fracture specimens, which are commonly utilized in fracture toughness testing of pipeline steels. Another is to quantify the potential coupling influence of specimen geometry and delamination size on crack-tip constraint by means of the J–Q theory thereby providing valuable insight into the effect of delamination cracks on macroscopic fracture behavior in conventional fracture specimens. Laboratory testing of an API 5L X70 steel at room temperature provides the mechanical properties used in the numerical analysis incorporating delamination cracks with varying sizes. Nonlinear finite element analyses of very detailed 3-D finite element models of C(T) and clamped SE(T) fracture specimens for the API X70 pipeline steel enable assessing the effects of prescribed delamination cracks on the crack front fields and constraint with increased deformation levels as characterized by the J-integral. Overall, the present analyses reveal important features of 3-D crack front fields in fracture specimens with a crack-divider delamination that have a direct bearing on the often observed toughness increase in fracture testing of materials with through-thickness anisotropy in mechanical properties.

1. Introduction

The growing demand for energy and natural resources has been pushing exploration and production activities of oil and natural gas in more hostile and remote environments. In particular, current trends in long distance, high pressure transmission gas pipelines favor the use of larger pipe diameters and increased operational pressure associated with high strength steel grades to reduce the pipe wall thickness. However, a different picture emerges in the case of deepwater subsea pipelines, including submarine risers and flowlines. Here, the high external pressures, often combined with large loads and displacements related to geohazard features of the natural seabed, dictate the use of heavy pipe wall thickness [1–4]. While recent developments in manufacturing and installation techniques enable the fabrication and laying of heavy wall pipeline systems for deepwater applications, structural integrity and toughness behavior of thick-wall subsea pipelines play a key role in fitness-for-service (FFS) and engineering critical assessment (ECA) procedures applicable to defect assessments of these structures with strong impact on their safe operation.

Thermo-mechanical control rolled processes (TMCP) represent a major production route for high strength, low allow (HSLA) pipeline grade steels as an advantageous technical and economical manufacturing method to achieve excellent strength/toughness combination in these materials. However, much previous research shows that HSLA steels produced by the TMCP process display marked anisotropy in microstructural and metallurgical features (see, for example, Tanaka [5] and Shah [6]) which strongly affects the mechanical and toughness behavior. More generally, these features involve the formation of an inhomogeneous distribution of inclusions and segregations with banding and elongated grain structure. Possibly the most important phenomenon associated with microstructural anisotropy in HSLA pipeline steels is the development of transverse delamination cracking (splits) along the rolling direction with important implications for testing of fracture toughness specimens as well as structural integrity assessments of flawed piping components. This type of delamination crack in TMCP steels is caused either by non-metallic inclusions or most

* Corresponding author.
E-mail address: claudio.ruggieri@usp.br (C. Ruggieri).

http://dx.doi.org/10.1016/j.ijpvp.2015.01.004
0308-0161/

often by cleavage cracking in the through-thickness direction due to some preferred orientation texture effects coupled with a high density of elongated ferrite grains [7,6,8]. Hence, the phenomenon of delamination fracture in this class of material may occur either in the earlier, lower grade pipeline steels, such as API X60 steel, produced by conventional thermomechanical rolling or in more advanced, higher grade materials, such as API X80 and X100 steel, produced by improved thermomechanical rolling with accelerated cooling.

Oil and gas pipelines, including piping components, have a history of strong safety records due to regulatory hydrostatic tests often required by pipeline design and safety standards (see, for example [9,10], for illustrative examples). These pressure tests reach hoop stress levels exceeding the material yield stress thereby ensuring that the pipeline contains virtually no preservice defects which might cause failure at its operating stress level when it is put into service [11]. Further, while there are few pipeline failures reported in the literature associated with transverse delamination cracking, most directly connected to full-scale burst tests [12,13], delamination fracture of the pipeline wall does not represent a major cause of pipeline failure [11]. Even when delamination in the mid-wall of the pipe leads to pipeline rupture caused by ductile fracture (see Ref. [14] for illustrative example), it is often produced by the diffusion of atomic hydrogen at inclusions in the pipe steel during normal pipeline operations, a mechanism known as hydrogen induced cracking (HIC) [15,16]. However, delamination cracking does affect fracture toughness values measured using laboratory fracture specimen thereby complicating the definition of meaningful fracture toughness data for application in fracture assessments of structural piping components. In particular, the increase in measured fracture toughness often observed in fracture testing of specimens in the transverse (L–T or T–L) direction is associated with a mechanism of crack-divider delamination toughening in which the formation of through-thickness splitting results in loss of through-thickness constraint [17]. Since laboratory testing of fracture specimens to measure crack growth resistance curves (generally termed R-curves) displays a marked effect of absolute specimen size/thickness on R-curves, the accurate evaluation of ductile crack growth in fracture specimens with transverse delamination cracking along the crack front and its subsequent application in safety assessment of piping components remain essential. As a step in this direction, we describe an extensive numerical investigation on delamination effects in conventional fracture specimens and implications for their macroscopic fracture behavior.

Considerable progress in understanding the mechanisms of delamination cracks in structural steels was achieved by means of detailed observations of fracture surfaces in tensile and impact specimens of hot-rolled steels (see, for example, [18–24]). These studies revealed a marked influence of delamination cracking on the ductile-to-brittle transition (DBT) behavior for these materials as the ductile–brittle transition shifts towards lower temperatures with increased number of fracture surface delaminations. Later, Guo et al. [25], Shin et al. [26,27] and Hong et al. [28] specifically investigated the delamination toughening mechanisms in pipeline grade steels, including API X70 and X80 steels, and indicated a potential strong interaction between the separation of transverse weak planes and the loss of stress triaxiality in the crack front region due to through-thickness splitting. More recently, Pyshmintsev et al. [13] provided strong evidence of the reduced resistance to ductile fracture propagation associated with delamination cracking based on modified Charpy tests conducted on an API X80 pipeline steel. These research efforts show the strong coupling between the onset of delamination cracks and cleavage or quasi-cleavage fracture associated with grain boundary embrittlement resulting from precipitates formed during the hot-rolling process. Work along parallel lines addressing delamination effects on fracture toughness behavior in other metallic alloys has also been conducted by Rao et al. [17] and Rao and Ritchie [29,30]. They provided clear indication that the increased fracture toughness properties in L–T orientation at low temperature for Al–Li alloys is primarily associated with the development of delamination cracks. More recently, Pilhagen and Sandstrom [31] examined the influence of delaminations on the measured fracture toughness of hot-rolled duplex stainless steels using standard SE(B) specimens tested at low temperatures.

While the general features of delamination effects on the measured fracture toughness for structural materials became qualitatively clear through these previous studies, further work remains to be done to quantify the rather complex interaction of transverse delamination cracks with the crack front of the macroscopic crack. Indeed, the increase in measured fracture toughness observed in fracture testing of specimens in the transverse (L–T or T–L) direction arises from a crack-divider delamination mechanism in which the incidence of through-thickness splitting changes the crack front (through thickness) constraint and provides an additional contribution to the total work of fracture. Clearly, the influence of through-thickness splitting is viewed as effectively dividing the bulk of the specimen into smaller sections of reduced thickness thereby relaxing the crack front stress triaxiality from predominantly plane-strain to nearer plane-stress conditions [17,29,30]. Recent work of Kalyanam et al. [32] addressed a numerical investigation of delamination cracking effects in Al–Li alloys to characterize the crack front stress-strain fields for 3-D, small scale yielding (SSY) finite element models with and without a delamination crack. However, in spite of the promise evident in this work, more systematic studies addressing the interconnection of the controlling mechanical features - delamination size and crack-tip constraint - and their relative contributions to the macroscopic fracture behavior remain relatively scarce.

Motivated by these observations, this work addresses a numerical investigation of the crack front fields and effects of crack-tip constraint in conventional fracture specimens with prescribed transverse delamination cracks. One purpose of this study is to conduct a systematic evaluation of delamination effects in side-grooved and plane-sided C(T) fracture specimens and a clamped SE(T) geometry; this latter configuration is now commonly utilized in fracture toughness testing of pipeline steels. Another is to quantify the potential coupling influence of specimen geometry and delamination size on crack-tip constraint by means of the J–Q theory thereby providing valuable insight into the effect of delamination cracks on macroscopic fracture behavior in conventional fracture specimens. Laboratory testing of an API 5L X70 steel at room temperature provides the mechanical properties used in the numerical analysis incorporating delamination cracks with varying sizes. Nonlinear finite element analyses of very detailed 3-D finite element models of C(T) and clamped SE(T) fracture specimens for the API X70 pipeline steel enable assessing the effects of prescribed delamination cracks on the crack front fields and constraint with increased deformation levels as characterized by the J-integral. The numerical simulations encompass typical, widely used specimen geometries, including a deeply-cracked C(T) configuration with crack size to specimen width ratio of $a/W = 0.65$ and a clamped SE(T) specimen with $a/W = 0.4$, both having 20% side-grooves (10% on each side). In these models, delamination fracture is modeled by introducing a delamination crack in the specimen center-plane region with a prescribed length, ℓ_D, and height, h_D, at the onset of loading. The extensive numerical analyses performed here reveal important features of 3-D crack front fields in fracture specimens with transverse delamination cracks that give

additional insight into the delamination cracking behavior of materials with through-thickness anisotropy in mechanical properties.

2. Delamination cracking in fracture testing of an API X70 pipeline steel

Hippert [33] performed extensive fracture toughness tests at room temperature (20 °C) on side-grooved C(T) fracture specimens with $a/W = 0.65$ in the T-L orientation to measure crack growth resistance properties using the unloading compliance procedure [34,35]. The geometry and dimensions of the tested C(T) specimen follow ASTM E1820 [36] with $B = 25.4$ mm and $W = 50.8$ mm. Here, a is the crack size, W denotes the specimen width and B represents the specimen thickness. After fatigue precracking, the specimens were side-grooved to a net thickness, B_N, of 20 mm (10% side-grooves on each side of the specimen) and tested following the requirements of ASTM E1820 standard [36]. The material is a control-rolled API 5L X70 pipeline grade steel with 484 MPa yield stress (σ_{ys}) and 590 MPa tensile strength (σ_{uts}) at room temperature with relatively moderate-to-low hardening properties ($\sigma_{ys}/\sigma_{uts} \approx 0.82$), Young's modulus, $E = 205$ GPa, and Poisson's ratio $\nu = 0.3$. Hippert and Ruggieri [37] provide the engineering stress-strain curve for the tested steel (average of two tests) obtained from mechanical tensile tests conducted on longitudinal tensile specimens (ASTM E8 [38]). Since the tested API X70 steel exhibits a discontinuous, albeit relatively small, yielding in the measured engineering $\sigma-\varepsilon$ curve, this yield stress value corresponds to the upper yield strength recorded in the test, which differs only slightly from the lower yield strength measured within the yield plateau. Hippert and Ruggieri [37] provide additional details of the fracture tests, material properties and chemical composition, including the metallographic analysis, for the tested pipeline steel.

Fig. 1(a) shows the measured records of load versus load line displacement (LLD or Δ) obtained for two representative test specimens; essentially similar load–displacement data are observed for other test specime n Fig. 1(a). Fig. 1(b) displays the corresponding crack growth resistance curves (also termed R-curves) derived from the load–displacement records using the unloading compliance procedure and related formulations provided in ASTM E1820 [36]. Limiting attention to the load–displacement curve displayed in Fig. 1(a), it can be seen that a number of load drops take place with increased load line displacement during the fracture test. Observe that the first major pop-in load drop occurs near the maximum load attained in the test for both specimens. Such behavior is attributed primarily to the occurrence of extensive delamination fracture (splitting) perpendicular to the crack plane. Now focus attention on the resistance curves shown in Fig. 1(b). At the amount of ductile tearing $\Delta a \approx 0.5 \sim 0.8$ mm (which corresponds to Δa-values just after the onset of stable crack growth), both curves appear to separate from each other as a probable result of the major load drops observed in the corresponding load–displacement records shown in Fig. 1(a). Here, while the J–R curves appear to be less affected by the delamination cracking observed in the tested specimens, it should be cautioned that a load drop in the P–Δ curve does not translate directly into a sudden change in the crack growth resistance curve. Since J derives from the total plastic area computed at each unloading point in the P–Δ curve (see, e.g., Anderson [35]), its value tends to change gradually rather than abruptly following the onset of a delamination. Moreover, delamination cracking is also likely to further contribute to the inherent scatter in the data set instead of a smooth resistance curve. Indeed, Silva et al. [39] provide crack growth resistance curves for an API X80 steel which display very large scatter in the data set as a result of severe multiple delamination fracture which takes place during the fracture testing.

Fractographic examination of the fracture toughness test pieces revealed the presence of delamination cavities characterized by small splits in the fracture surface of the specimens, which are likely to act as precursors of the larger macroscopic delamination cracks. Fig. 2(a) displays a typical fracture surface for the tested C(T) specimens with multiple delamination fractures normal to the crack plane. Here, larger delamination cracks are primarily formed along the direction of crack propagation, mostly at the mid-thickness region, and accompanied by several small secondary cracks. A closer examination by SEM fractography shown in Fig. 2(b–c) reveals that these delamination cavities occur by a cleavage failure mode. In particular, Fig. 2(c) clearly shows well-defined cleavage planes characteristic of stress-controlled cleavage fracture at the edge of the delamination cavity under a much larger magnification.

Much of this fracture behavior can explained in terms of the connection between transverse delamination cracking and the anisotropic microstructural features of the material which govern the separation of transverse weak planes. Experimental observations [5,6,24] suggest that elongated grains resulting from hot rolling and densely aligned brittle precipitates along the grain boundaries represent the primary sources for the formation of delamination cracks. Under increased loading, the near-tip stresses acting along the through-thickness direction (Z) reach a critical value [20,40] thereby causing fracture of the weak planes (most often by a transgranular cleavage mechanism) and creating a macroscopically transverse planar crack. It is evident that the

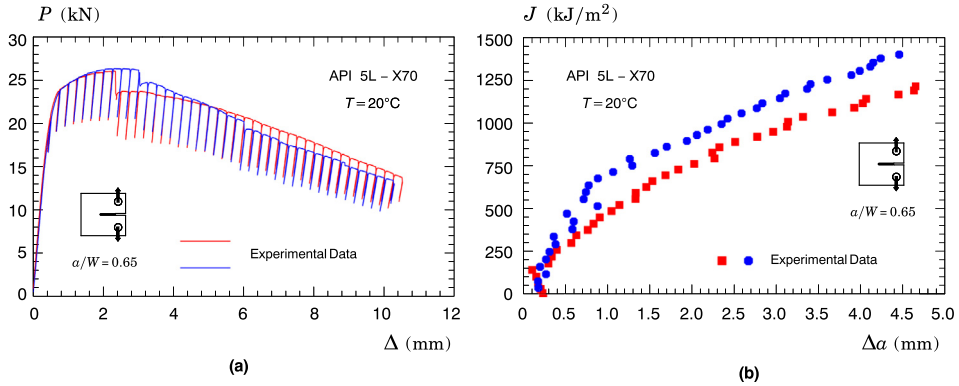

Fig. 1. (a) Measured load-LLD curve for the tested API X70 pipeline steel at room temperature using 20% side-grooved, 1-T C(T) specimens with $a/W = 0.65$ [33]; (b) Corresponding crack growth resistance curves derived from using the unloading compliance procedure according to ASTM E1820 [36].

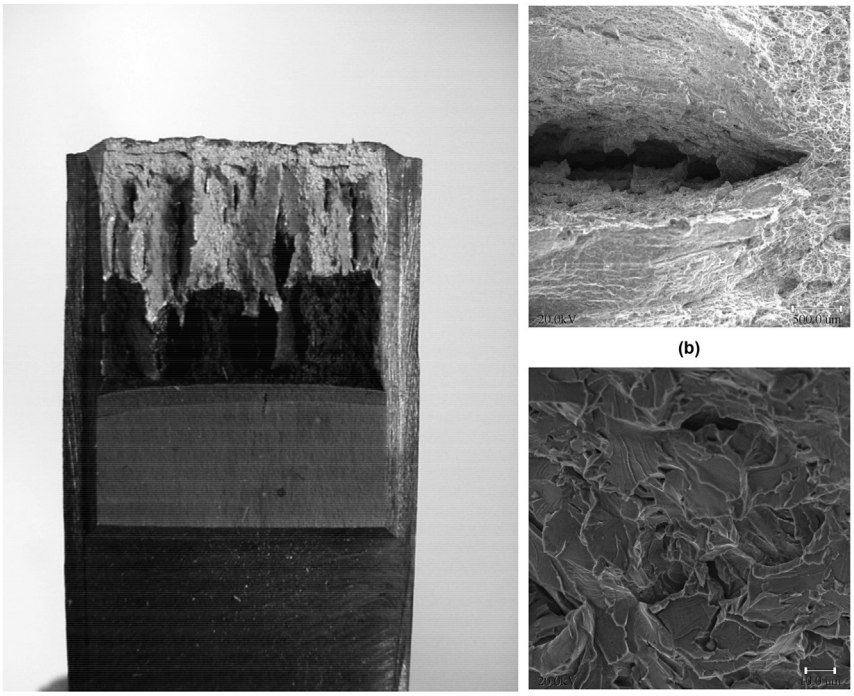

Fig. 2. (a) Macrofractograph of the fracture surface for a broken C(T) specimen showing the development of large delamination cracks perpendicular to the fracture surface reported by Hippert [33]; (b) SEM fractograph of the delamination cavity formed by material separation (split); (c) Well-defined cleavage planes characteristic of stress-controlled cleavage fracture at the edge of the delamination cavity.

through-thickness splitting causes the bulk of the specimen to be divided into thinner ligaments defined by the delamination cracks thereby relaxing the near-tip stresses which drive the cleavage fracture process and, further, affecting strongly the crack-front size over which high levels of near-tip stress triaxiality (constraint) are maintained.

These changes in the crack-tip stress fields following the onset and subsequent development of delamination cracks along the crack front are plausibly dependent on the delamination size. To address this issue, the present study considers very detailed numerical models of the tested C(T) specimen, including further analyses incorporating a low constraint specimen geometry, to resolve the crack-front fields that evolve during the development of transverse delamination cracks. The results which follow provide valuable insight and additional understanding of the role of delamination cracking on the measured fracture toughness for the tested pipeline steel.

3. Description of crack-front constraint: the $J-Q$ approach

The assessment of specimen geometry and loading mode (bending vs. tension) effects on fracture behavior for structural steels in the ductile-to-brittle (DBT) transition has received considerable attention in recent years. At increased loads in a finite body, such as a cracked specimen or structure, the initially strong high constraint fields under well-contained plasticity gradually change to fields under large scale yielding (LSY) as crack-tip plastic zones increasingly merge with the global bending yielding on the nearby traction free boundaries. This phenomenon, often termed loss of constraint, contributes to the apparent increased toughness observed in fracture testing of shallow cracked and tension loaded geometries [41,42]. While a number of approaches have been proposed to describe effects of constraint changes on fracture behavior, the present work focuses on a widely adopted methodology to quantify the evolving level of stress triaxiality ahead of the crack front under increased remote loading based upon the $J-Q$ framework. This section introduces the essential features of the methodology needed to assess delamination cracking effects on crack front stress triaxiality in the analyzed fracture specimens.

Development of a two-parameter characterization of the elastic–plastic crack-tip fields begins by considering a cracked body subjected to a remote stress in which crack-tip deformation scales with J/σ_0 where J denotes Rice's J-integral [43] and σ_0 is a reference (yield) stress. At load levels sufficiently small so that crack-tip plasticity is limited, it can be shown that the mode I plane-strain elastic–plastic near-tip fields can be described by a single family of crack-tip fields with varying stress triaxiality. These arguments motivated O'Dowd and Shih (OS) [44,45] to propose an approximate two-parameter description for the elastic–plastic crack tip fields based upon a triaxiality parameter more applicable under large scale yielding (LSY) conditions for materials with elastic–-plastic response described by a power hardening law given by $\varepsilon/\varepsilon_0 \propto (\sigma/\sigma_0)^n$. Here, n denotes the strain hardening exponent, σ_0 and ε_0 are the reference (yield) stress and strain, respectively. Guided by detailed numerical analyses employing a modified boundary layer (MBL) model, originally proposed by Rice [46], OS [44,45] identified a family of self-similar fields in the form

$$\sigma_{ij} = \sigma_0 f_{ij}\left(\frac{r}{J/\sigma_0}, \theta, Q\right) \tag{1}$$

where the dimensionless second parameter Q defines the amount by which σ_{ij} in fracture specimens differ from the adopted reference SSY solution with the T-stress term [47–50] set to zero. In the above Eq. (1), r and θ are polar coordinates centered at the crack tip with $\theta = 0$ corresponding to a line ahead of the crack.

Limiting attention to the forward sector ahead of the crack tip between the SSY and the fracture specimen fields, OS showed that $Q\sigma_0$ corresponds effectively to a spatially uniform hydrostatic stress, i.e., the difference field relative to a high triaxiality reference stress state

$$(\sigma_{ij})_{FB} = (\sigma_{ij})_{SSY} + Q\sigma_0\delta_{ij} \tag{2}$$

where the dimensionless second parameter Q defines the amount by which σ_{ij} in fracture specimens, $(\sigma_{ij})_{FB}$, differ from the adopted high triaxiality reference SSY solution, $(\sigma_{ij})_{SSY}$. Consequently, Q is often defined as

$$Q \equiv \frac{(\sigma_{yy})_{FB} - (\sigma_{yy})_{SSY}}{\sigma_0} \tag{3}$$

where the difference field described in terms of the opening (Mode I) stresses, σ_{yy}, is conventionally evaluated at the normalized crack-tip distance $\bar{r} = r/(J/\sigma_0) = 2$, which represents a microstructurally significant distance ahead of crack tip related to the operative fracture mechanism. OS [44,45], Dodds et al. [51] and Cravero and Ruggieri [52] have also shown that Q is relatively independent of $\bar{r}$ in the range $1 \le \bar{r} \le 5$. Construction of J–Q trajectories for structural components and fracture specimens then follows by evaluation of Eq. (3) at each stage of loading in the finite body.

4. Finite element procedures and geometric models

4.1. C(T) and clamped SE(T) fracture specimens

Nonlinear numerical analyses are conducted on very detailed 3-D finite element models for the side-grooved 1-T C(T) specimen with $a/W = 0.65$ utilized in the fracture testing briefly described in Section 2. The geometry, size and material flow properties match those for the C(T) configuration tested in the experiments performed by Hippert [33] and Hippert and Ruggieri [37]. Fig. 3(a) shows the finite element model constructed for analyses of the tested C(T) specimen having a 20% side-groove (10% on each side). The side-grooves are introduced in the numerical model as follows: 1) the Y-constraints on crack-plane nodes for which $X = 0$ and $Z > 0.4B$ (these nodes correspond to the 4 outermost layers) are first released; 2) these nodes are translated in the Y direction according to a linear mapping corresponding to a side-groove half-angle of 30°. Since the primary interest here lies in the coupled effect of side-grooves and a center-plane delamination crack on crack-front constraint, the notch radius of the side-groove is not modeled. Moreover, to examine the potential effects of side-grooves on crack-front constraint for numerical models with a center-plane delamination crack, the finite element analyses also consider the previous 3-D numerical models for the 1-T C(T) specimens but with conventional, plane-sided configuration (no side-groove). These finite element models have similar mesh arrangement and mesh details as already described for the 20% side-grooved specimens.

Modeling of the center-plane delamination crack requires a very refined crack-front mesh to adequately characterize the stress-free delamination surface and to accurately resolve the crack-front stress fields (see further details next in Section 4.2). A conventional mesh configuration having a focused ring of elements surrounding the crack front is used with a small blunt notch at the crack tip; the radius of the blunt notch, ρ_0, is 2.5 μm (0.0025 mm). Symmetry conditions enable analyses using one-quarter of the 3-D models with appropriate constraints imposed on the symmetry planes. The finite element mesh has 16 variable thickness layers defined over the half net thickness ($B_N/2$) to accommodate strong Z variations in the stress distribution and at the same time to resolve the steep stress gradients near the center-plane delamination crack. Here, the layer thickness defining the delamination crack at $Z = 0$ is $0.005B_N$ whereas the layer defined near the side-groove

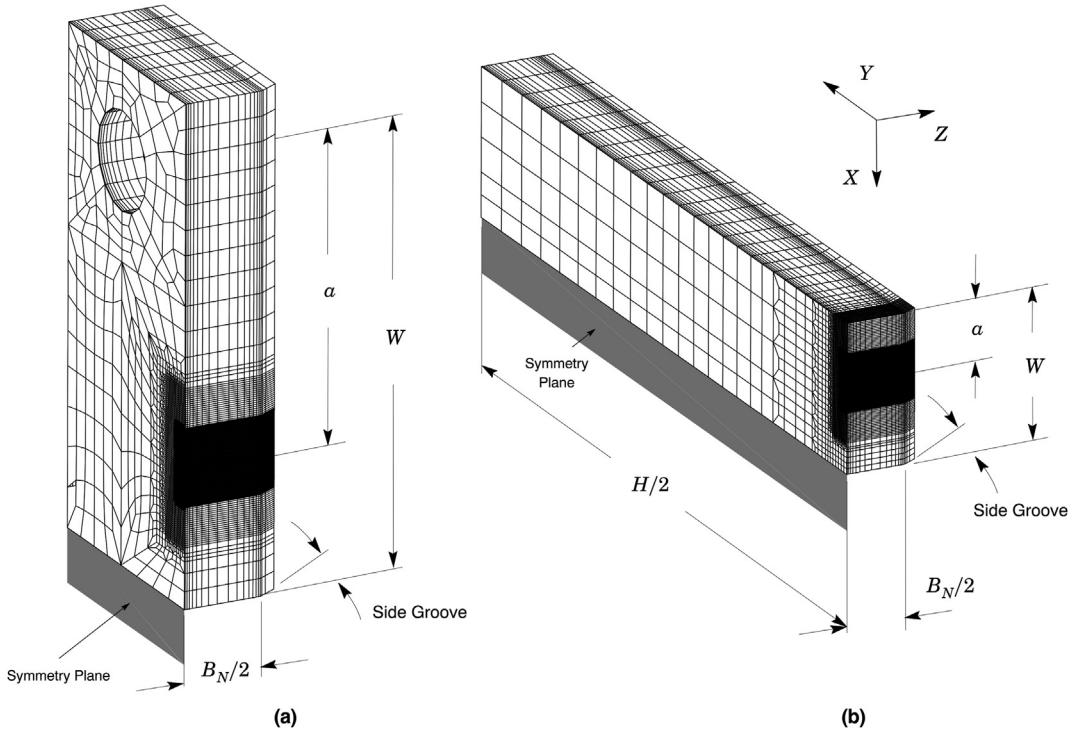

Fig. 3. (a) Quarter-symmetric finite element model used in the 3-D analyses of the tested C(T) specimen with $a/W = 0.65$ and 20% side-groove (10% on each side of specimen surface); (b) Quarter-symmetric 3-D finite element model of the 20% side-grooved, clamped SE(T) specimen with $a/W = 0.4$.

($Z = B_N/2$) is $0.012B_N$. The additional 4 outermost layers then compose the full bulk of the specimen, $B/2$, as indicated in Fig. 3(a). The quarter-symmetric, 3-D model for this specimen has 183,280 nodes and 171,000 8-node, 3-D elements. These finite element models are loaded by displacement increments imposed on the top nodes of the loading pin hole to enhance numerical convergence with increased loading and plastic deformation.

Nonlinear finite element analyses are also described for single edge notch tension SE(T) specimens under clamp conditions having a crack size over specimen width ratio of $a/W = 0.4$. This specimen geometry has been increasingly utilized to measure crack growth resistance curves more applicable to high pressure piping systems, including girth welds of marine steel risers. In particular, a number of defect assessment procedures for girth weld pipelines, including DNV F101 [10] and DNV F108 [53], specify the use of clamped SE(T) specimens with $H/W = 10$ and $W = B$ configuration, where H is the distance between the clamped ends and the thickness, B, represents the pipe wall thickness (see Refs. [54,55] for additional details on this specimen geometry). To make contact with the numerical analyses performed on the 1-T C(T) specimens, the finite element model constructed for the clamped SE(T) configuration has thickness, $B = 25.4$ mm, and 20% side-grooves (10% on each side). Fig. 3(b) shows the quarter-symmetric, 3-D model for this geometry with 16 variable thickness layers defined over the half net thickness ($B_N/2$), 191,688 nodes and 179,000 8-node, 3-D elements. This numerical model also has similar mesh arrangement and mesh details as already described for the 1-T C(T) specimens, including the center-plane delamination crack model, with displacement increments imposed on the loading points to enhance numerical convergence with increased levels of deformation.

4.2. Finite element modeling of center-plane delamination cracks

Following the discussion provided in previous Section 2, we idealize the delamination fracture process by introducing a delamination crack in the specimen center-plane region with a prescribed length, ℓ_D, and height, h_D, at the onset of loading as depicted in Fig. 4(a). Within the present simplification, the delamination crack is viewed as a thin rectangular slab embedded into the specimen centerplane and centered at the crack tip.

Fig. 4(b) shows the highly refined finite element mesh defining the delamination crack region in which the size of the square elements within the thin slab is 0.025 mm. The *physical* delamination crack is introduced into the model by releasing the X and Z-constraints on the nodes defining the delamination crack region (refer also to Fig. 3). Guided by experimental observations made by Hippert [33], the delamination sizes (as characterized by the length, ℓ_D, and the height, h_D) adopted in the present study are taken as 5×2.5 mm, 10×5 mm and 20×10 mm. This range of sizes provides a close representation of the observed delamination crack sizes and shapes with increased load levels up to a maximum J-value of 500 kJ/m^2 which is in accord with the onset of ductile tearing measured in the fracture testing conducted by Hippert [33]; indeed, Hippert and Ruggieri [37] report the toughness value at initiation of stable crack growth as $J_{Ic} = 440$ kJ/m^2. Moreover, while the adopted approach does not consider the growth of the delamination crack with increased loading, thereby not including history effects on the evolving crack front stress fields and crack front constraint, it is adequately descriptive of the local conditions affecting macroscopic fracture behavior in conventional fracture specimens with a crack-divider (transverse) delamination.

4.3. Material model and solution procedures

The analyses for delamination effects on crack front fields described next utilize an elastic–plastic constitutive model with J_2 flow theory and conventional Mises plasticity in small geometry change (SGC) setting. The numerical solutions employ a simple power-hardening model to characterize the uniaxial true stress *vs.* logarithmic strain in the form

$$\frac{\overline{\varepsilon}}{\varepsilon_0} = \frac{\overline{\sigma}}{\sigma_0}, \quad \overline{\varepsilon} \le \varepsilon_0; \quad \frac{\overline{\varepsilon}}{\varepsilon_0} = \left(\frac{\overline{\sigma}}{\sigma_0}\right)^n, \quad \varepsilon > \varepsilon_0 \tag{4}$$

where σ_0 and ε_0 are the reference stress and strain, and n denotes the strain hardening exponent. In the present context, the reference stress is taken as the yield stress so that $\sigma_0 \equiv \sigma_{ys}$. As already described, the tested API X70 pipeline grade steel has 484 MPa yield stress (σ_{ys}) and 590 MPa tensile strength (σ_{uts}) at room temperature (20 °C) with relatively moderate-to-low hardening properties ($\sigma_{ys}/\sigma_{uts} \approx 0.82$), Young's modulus $E = 205$ GPa and Poisson's ratio $\nu = 0.3$. A piecewise-linear representation of the measured engineering stress-strain data converted to true stress-logarithmic strain data [56] describes the flow properties for the numerical analyses conducted here.

The adopted material model deserves further consideration since it is at the heart of the numerical solutions generated for the crack-tip stress fields, including the J–Q trajectories, presented next. Ideally, accurate descriptions of fields near the zone of finite strains would be desirable in some applications, in which case large geometry change (LGC) analysis is required to describe the intense strain concentration directly ahead of the crack tip. However, outside the crack-tip blunting zone, the LGC and SGC stresses converge to very similar values as demonstrated by several

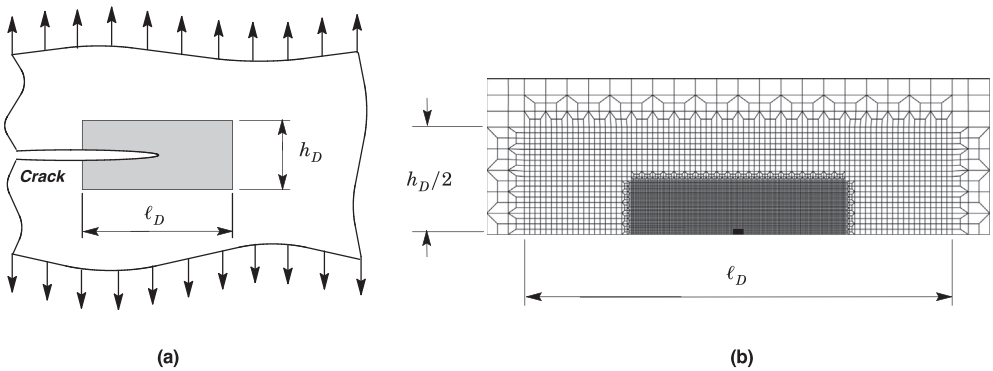

Fig. 4. (a) Schematic for the adopted geometry of the transverse rectangular delamination with length, ℓ_D, and height, h_D; (b) Finite element model of the transverse rectangular delamination.

previous works (see, e.g., Dodds et al. [57]). As will be shown later, the crack-tip stresses and parameter Q are extracted at the normalized crack-tip distance, $r/(J/\sigma_0) = 2$, which corresponds approximately to 4 × CTOD for this material [35,58]; hence, it is sufficiently far from the crack tip to avoid the strong blunting effects on the crack-tip stress fields. Consequently, the SGC analyses prove highly adequate for the present study while, at the same time, eliminating potential numerical difficulties related to convergence of the highly refined numerical models employed. It is also of interest to note that, since parameter Q quantifies the *relative* difference field between the finite cracked body and a high triaxiality reference stress state, differences between the SGC and LGC solutions remain small.

The finite element code WARP3D [59] provides the numerical solutions for the 3-D analyses reported here. Evaluation of the J-integral derives from a domain integral procedure [60] which yields thickness average values for J retaining strong path independence for domains defined outside the highly strained material near the crack tip. Such J-values also agree very well with estimation schemes based upon η-factors for deformation plasticity [35] so that they provide a convenient parameter to characterize the average intensity of far field loading on the crack front. The code formulates and solves the equilibrium equations at each iteration using parallel algorithms and implements the so-called $\overline{B}$ formulation (see Ref. [59] for details) to preclude mesh lock-ups that arise as the deformation progresses into fully plastic, incompressible modes.

The SSY reference fields required to construct the J–Q trajectories addressed in Sections 5.1.3 and 5.2 are derived from plane-strain, finite element solutions of a modified boundary layer (MBL) model consisting of a (very large) circular region containing an edge crack [41,42,46,61]. With the plastic region limited to a small fraction of the domain radius, $R_p < R/20$ where R_p is the radius (size) of the crack-tip plastic zone, the general form of the asymptotic crack-tip stress fields well outside the plastic region is given by William's expansion [62] as

$$\sigma_{ij} = \frac{K_I}{\sqrt{2\pi r}} f_{ij}(\theta) \tag{5}$$

where K_I is the elastic stress intensity factor, f_{ij} define the angular variations of in-plane stress components and (r,θ) are polar coordinates centered at the crack tip. Numerical solutions for different levels of parameters $K_I = \sqrt{EJ/(1-\nu^2)}$ are generated by imposing the corresponding displacements of the elastic, Mode I singular field on the outer circular boundary ($r = R$) which encloses the crack [42]. The research code FRACTUS2D [63] is employed to compute J–Q trajectories derived from the extensive 3-D analyses for the analyzed fracture specimens.

In the present investigation, a requisite feature to obtain accurate numerical descriptions of the crack-tip stress fields which are accurate over distances of order a few CTODs and, at the same time, reflect the near-tip perturbations introduced by the prescribed delamination model is the use of a highly refined near-tip mesh of numerically efficient 8-node, 3-D elements (see details of the element formulation in Ref. [59]). A weak, implicit length-scale enters the finite element computations through the near-tip mesh size as insufficient mesh refinement reduces the stress values ahead of the crack front, especially at smaller load levels. However, the 3-D models used in this study possess the required level of mesh refinement to resolve accurately the crack-tip stresses to characterize very well the effects of prescribed delamination cracks on the crack front fields and constraint with increased deformation levels.

5. Results and discussion

The following sections provide key results derived from the extensive finite element analyses conducted on the C(T) and SE(T) specimens with delamination cracks. Attention is directed to the changes in crack-front stress fields and crack-front constraint with increased macroscopic loading (as characterized by increased values of J in the present study) with varying delamination sizes. Although several experimental studies show the strong influence of delamination toughening mechanisms on the measured fracture toughness of pipeline steels and structural materials, a systematic investigation on the interaction of transverse delamination cracks with the macroscopic crack in common fracture specimens and implications for the crack-front stress fields and crack-front constraint remain relatively rare.

The presentation considers 3-D models with delamination cracks characterized by a defined rectangular-shaped strip with varying length over height (ℓ_D/h_D) ratios as introduced in Section 4.2. The results include the coupling effects of delamination crack and side-groove on crack-front stress fields and crack-front constraint for the C(T) specimen. The analyses also explore the fracture behavior of a low constraint, side-grooved SE(T) crack configuration with delamination cracks and how it compares with the tested C(T) specimen. Moreover, to assess delamination effects on crack front stress fields and local values of J, the deformation levels range from small scale yielding conditions to fully yielded conditions and take the values, $J = 50$, 100, 250 and 500 kJ/m^2. In particular, $J = 250$ kJ/m^2 corresponds to a crack tip deformation limit, $M = (W-a)\sigma_0/J \approx 60$, relative to crack length, specimen thickness and remaining ligament, and $J = 500$ kJ/m^2 approximately defines the onset of ductile tearing measured in the fracture testing conducted by Hippert [33] as noted before.

5.1. Delamination effects in C(T) specimens

5.1.1. 3-D crack front stress fields

Fig. 5 shows the distribution of near-tip opening stresses, σ_{yy}, with increased levels of deformation, as characterized by J, for the side-grooved C(T) models with no delamination and with a delamination crack of 20 × 10 mm. In these plots, the opening stresses are normalized by the material yield stress, σ_0, and crack-tip distances are normalized by J/σ_0. The opening stresses are extracted from the nearest layer to the specimen centerplane which does not contain a delamination crack ($Z/(B_N/2) = 0.01$). Opening stresses of about 3.5 σ_0 are achieved at the normalized distance of $r/(J/\sigma_0) = 1$ for the model without a delamination crack which is characteristic of low-to-moderate hardening materials under well-contained and moderate yielding conditions [64,65]. By contrast, the opening stresses for the specimen with the center-plane delamination crack fall precipitously, so that they never exceed the yield stress value, σ_0, over crack-tip distances larger than physically relevant length scales associated with crack-tip blunting ($r/(J/\sigma_0) \geq 1$. Essentially similar trends are observed for other numerical models and delamination crack sizes; to conserve space, these results are not shown here.

Figs. 6–7 display the development of out-of-plane stresses, σ_{zz}, with increased load levels for the analyzed C(T) models with and without transverse delamination cracks. In these plots, the opening stresses are extracted at the normalized crack-tip distance, $r/(J/\sigma_0) = 2$, which corresponds approximately to 4 × CTOD for this material [35,58]. Consider first the results for the plane-sided C(T) specimens displayed in Fig. 6. The distribution of σ_{zz} over the crack front shown in Fig. 6(a) for the model without a delamination crack reveals maximum values over a relatively large fraction of the specimen thickness extending from midplane and then gradually

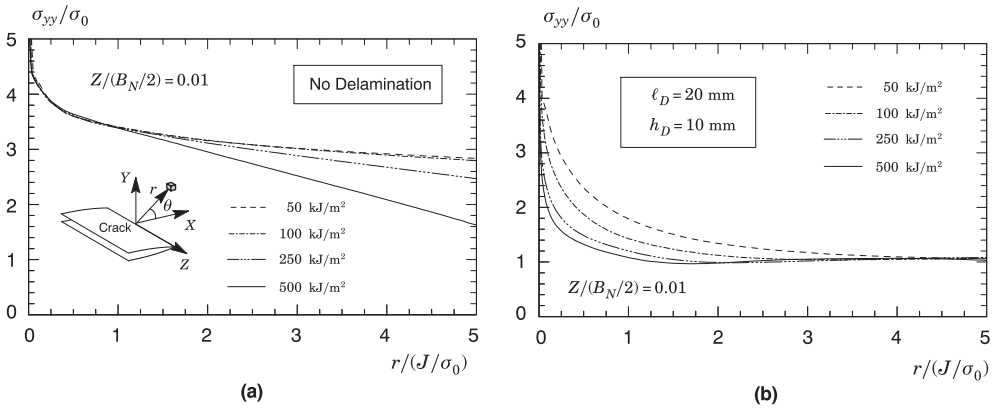

Fig. 5. Distribution of near-tip opening stresses (σ_{yy}) with increased deformation levels, as characterized by J, at the nearest layer to the specimen centerplane which does not contain a delamination crack ($Z/(B_N/2) = 0.01$) and $\theta = 0$ for the C(T) model with 20% side-grooves: (a) No delamination; (b) 20 × 10 mm delamination.

decreasing as the stress-free surface is approached; observe, however, that the stress gradient over the crack front is more pronounced with increased J-values as global bending field impinges strongly on the crack-tip fields and large scale yielding interacts with the stress-free specimen surface. A different picture emerges for models having a center-plane delamination crack with varying sizes shown in Fig. 6(b–d). Here, the introduction of a delamination crack now creates a stress-free surface at the centerplane thereby relaxing the through-thickness constraint and, at the same time, shifting the near-tip highly stressed region to the middle portion of the remaining thickness ligament (this corresponds approximately to $Z/(B/2) \approx 0.4 \sim 0.5$). Further observe that, apart from minor differences in the stress levels, the distributions of transverse stress, σ_{zz}, change only slightly with increased delamination sizes. Kalyanam et al. [32] report crack front stress distributions derived from 3-D small scale yielding (SSY) models with prescribed delamination crack sizes which exhibit similar trends to those shown here.

Now direct attention to the results for the side-grooved C(T) specimens displayed in Fig. 7. While the general effects of a delamination crack on the crack front stress fields are broadly consistent with the stress distributions shown in previous Fig. 6, inclusion of side-grooves does change the distribution of σ_{zz} over the crack front for the models with and without transverse delamination cracks. Fig. 7(a) shows that side-grooves maintain high levels of out-of-plane stress (essentially similar to the level attained at the specimen midplane) over a significant portion of the specimen thickness. When a delamination crack is introduced into

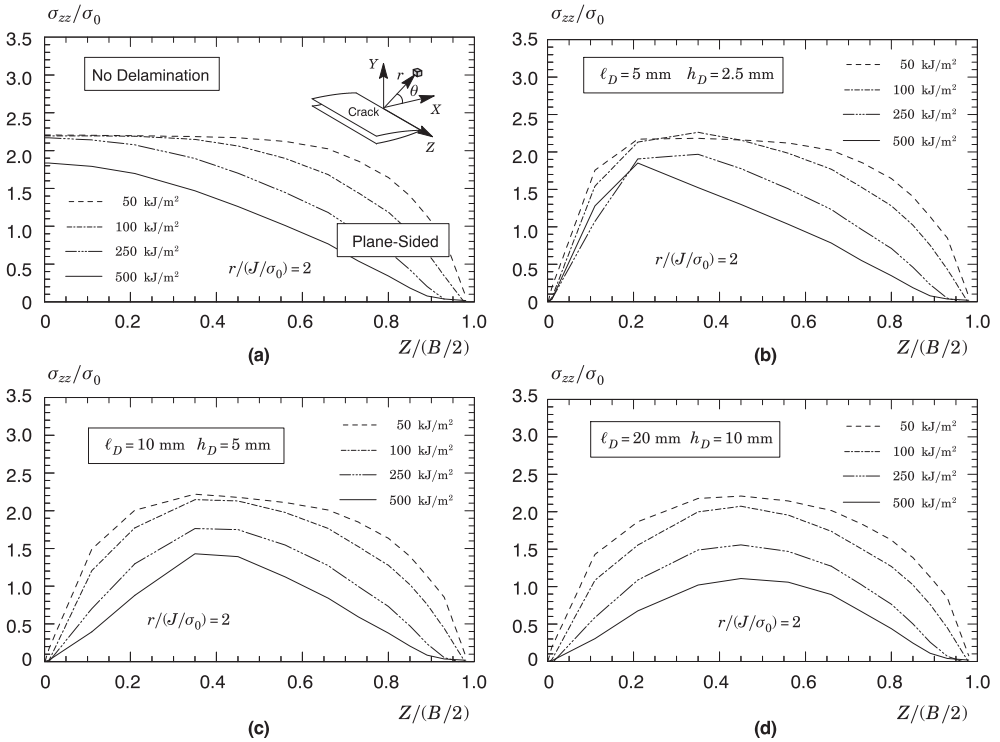

Fig. 6. Distribution of out-of-plane stresses (σ_{zz}) over the crack front with increased load levels at the normalized crack-tip distance, $r/(J/\sigma_0) = 2$ for the plane-sided C(T) model: (a) No delamination; (b) 5 × 2.5 mm delamination; (c) 10 × 5 mm delamination; (d) 20 × 10 mm delamination.

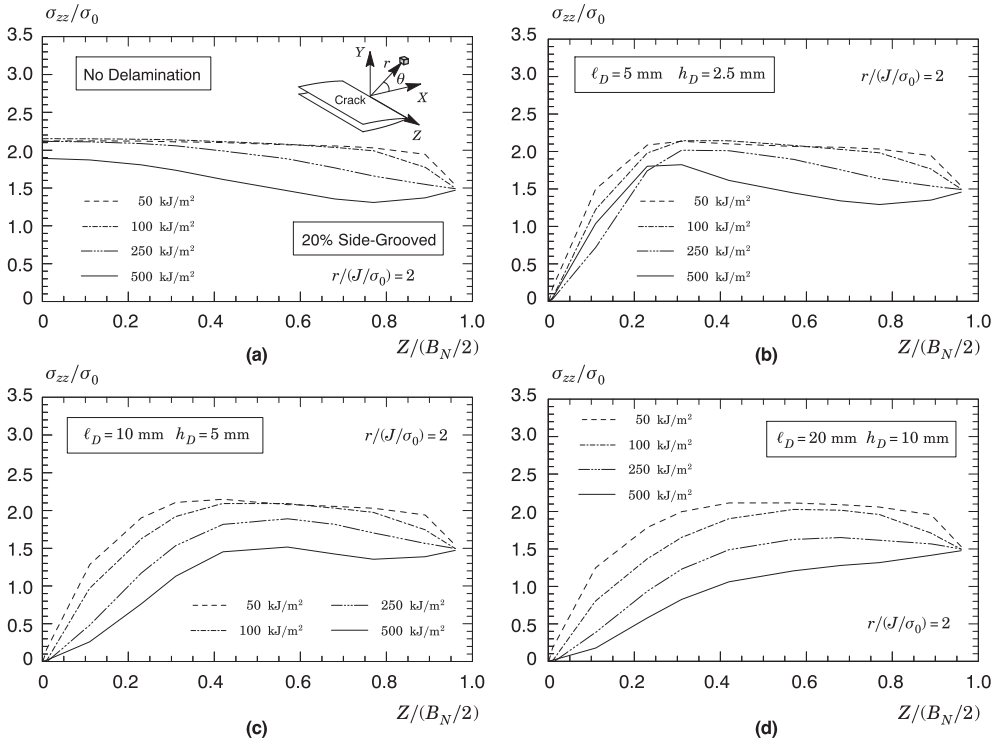

Fig. 7. Distribution of out-of-plane stresses (σ_{zz}) over the crack front with increased load levels at the normalized crack-tip distance, $r/(J/\sigma_0) = 2$ for the C(T) model with 20% side-grooves: (a) No delamination; (b) 5 × 2.5 mm delamination; (c) 10 × 5 mm delamination; (d) 20 × 10 mm delamination.

the model, the stress-free surface at $Z = 0$ relaxes the midplane stress, σ_{zz}, to zero but with a relatively weak effect on the stress distribution over the remaining thickness ligament, particularly for small delamination crack sizes, as shown in Fig. 7(b–d).

5.1.2. Variation of the J-Integral over the crack front

Figs. 8–9 display the distribution of J over the crack front, denoted J_{local}, with increased levels of loading for the models with and without transverse delamination crack. These J-values are

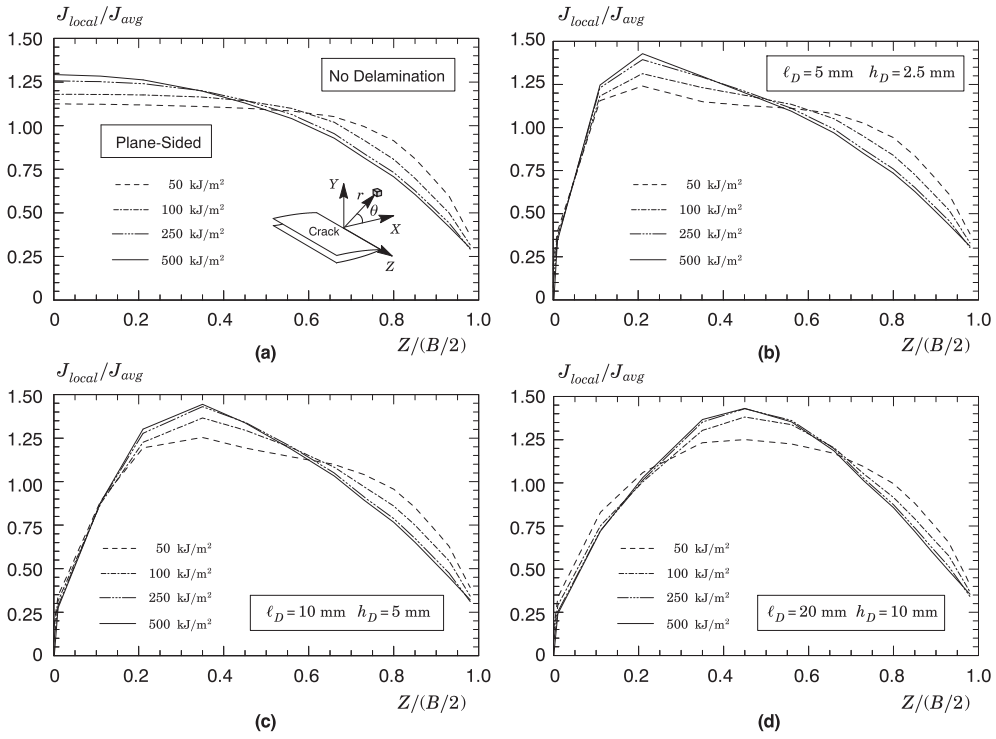

Fig. 8. Distribution of the J-integral over the crack front with increased deformation levels for the plane-sided C(T) model: (a) No delamination; (b) 5 × 2.5 mm delamination; (c) 10 × 5 mm delamination; (d) 20 × 10 mm delamination.

normalized by the thickness average values, denoted J_{avg}, so that the ratio J_{local}/J_{avg} defines the relative increase (decrease) of the local J-value with the thickness average J. Recall here that J_{avg} represents the conventional J-value that would be measured in fracture testing using a plastic η-factor as outlined previously in Section 4.3. The results shown in Fig. 8(a) corresponding to the plane-sided C(T) model without a delamination crack reveals that the maximum J-value occurs over a relatively small portion of the specimen centerplane region ($0 \le Z/(B/2) \le 0.4$) and then gradually decreases to much lower J-values as the stress-free surface is approached. For the side-grooved model, the distributions of J across the specimen thickness shown in Fig. 9(a) becomes nearly uniform for the entire range of deformation over a much larger portion of the crack front, as much as $0 \le Z/(B_N/2) \le 0.6 \sim 0.7$. This behavior is entirely consistent with other previous studies, including the work of Nevalainen and Dodds [42].

The results for the numerical models incorporating a delamination crack with varying sizes displayed in Figs. 8(b–d) and 9(b-d) share similar gross features as those already observed in previous Section 5.1.1. Here, the J-values at the centerplane drop precipitously to attain essentially similar levels as those corresponding to the stress-free surface for both the plane-sided and side-grooved models. Observe, however, that the J-distributions for the plane-sided C(T) specimen peak over a relatively narrow portion of the thickness ligament ranging from $Z/(B/2) \approx 0.25$ for the smaller delamination crack to $Z/(B/2) \approx 0.5$ for the larger delamination crack. By contrast, the side-grooved C(T) geometry maintains larger J_{local}/J_{avg}-ratios over a substantial part of the specimen thickness, particularly for small-to-moderate delamination crack sizes (5×2.5 mm and 10×5 mm delaminations).

5.1.3. Delamination effects on J–Q trajectories

Additional insight into the effects of delamination cracking on the crack front stress fields can be gained by examining the evolution of crack front stress triaxiality with increased deformation in terms of J–Q trajectories derived from the extensive 3-D analyses conducted on the C(T) fracture specimens with and without a delamination crack. Figs. 10 and 11 compare the effects of varying delamination sizes on the J–Q trajectories generated at selected locations along the crack front for the plane-sided and side-grooved C(T) specimens. Moreover, results derived from plane-strain analysis conducted for this configuration are also included in the plots for reference. In all plots, parameter Q is defined at the normalized distance ahead of crack tip given by $r/(J/\sigma_0) = 2$ whereas J is normalized by $(b\sigma_0)$ with b denoting the remaining crack ligament, $W-a$ (notice that we plot $J/(b\sigma_0)$ against negative values of Q to maintain positive scales). Further observe that the variation of Q along the crack front is plotted against increased macroscopic loading characterized in terms of thickness average value, J_{avg}. As already noted, parameter Q is relatively insensitive to the normalized crack-tip distance, $\bar{r}$, in the range $1 \le \bar{r} \le 5$ [44,45,51,52] so that these J–Q curves evaluated at $r/(J/\sigma_0) = 2$ characterize well the evolution of crack-tip constraint with increased loading for the analyzed C(T) geometry.

Figs. 10(a) and 11(a) show the evolution of Q with increased loading for the C(T) models without a delamination crack. These results reveal that the evolution of Q as loading progresses displays strong dependence on the crack front location. Here, the highest constraint levels are maintained at the specimen midplane in which the levels of crack-tip constraint are even higher than the corresponding constraint levels for the plane-strain condition. Observe that the Q-values for the $Z/(B/2) = 0.1$ ($Z/(B_N/2) = 0.1$) location (dashed line in the plot) are much higher than the plane-strain Q-values and only at the crack front location $Z/(B/2) = 0.4$ ($Z/(B_N/2) = 0.4$) the plane-strain results agree well with the 3-D J–Q trajectories. Such results follow very similar trends obtained in previous work of Nevalainen and Dodds [42] and Silva et al. [66]. Further observe that the J–Q trajectories for the side-grooved

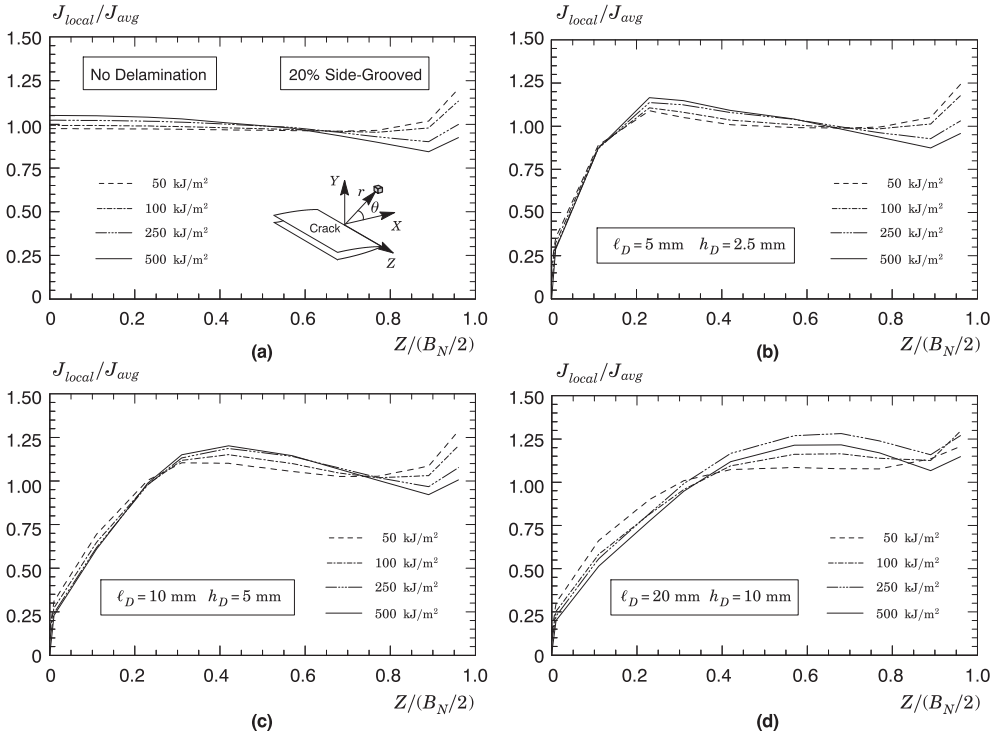

Fig. 9. Distribution of the J-integral over the crack front with increased deformation levels for the C(T) model with 20% side-grooves: (a) No delamination; (b) 5×2.5 mm delamination; (c) 10×5 mm delamination; (d) 20×10 mm delamination.

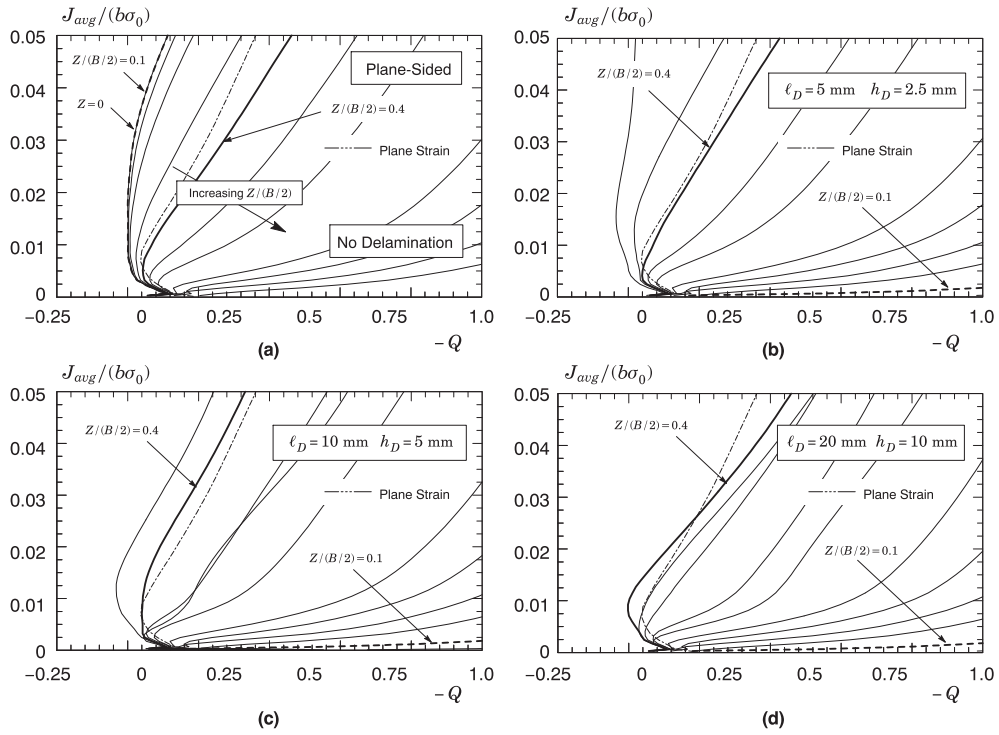

Fig. 10. J–Q trajectories at locations along the crack front for the plane-sided C(T) model: (a) No delamination; (b) 5 × 2.5 mm delamination; (c) 10 × 5 mm delamination; (d) 20 × 10 mm delamination.

model are less sensitive to the crack front location which is consistent with the results previously shown in Fig. 7(a) in which high levels of stresses are maintained over a significant portion of the specimen thickness.

Before proceeding with the results derived from the analyses for the models incorporating a delamination crack, we also draw attention to the proper interpretation of the J–Q curves displayed in Figs. 10(a) and 11(a). The analyses described here clearly show

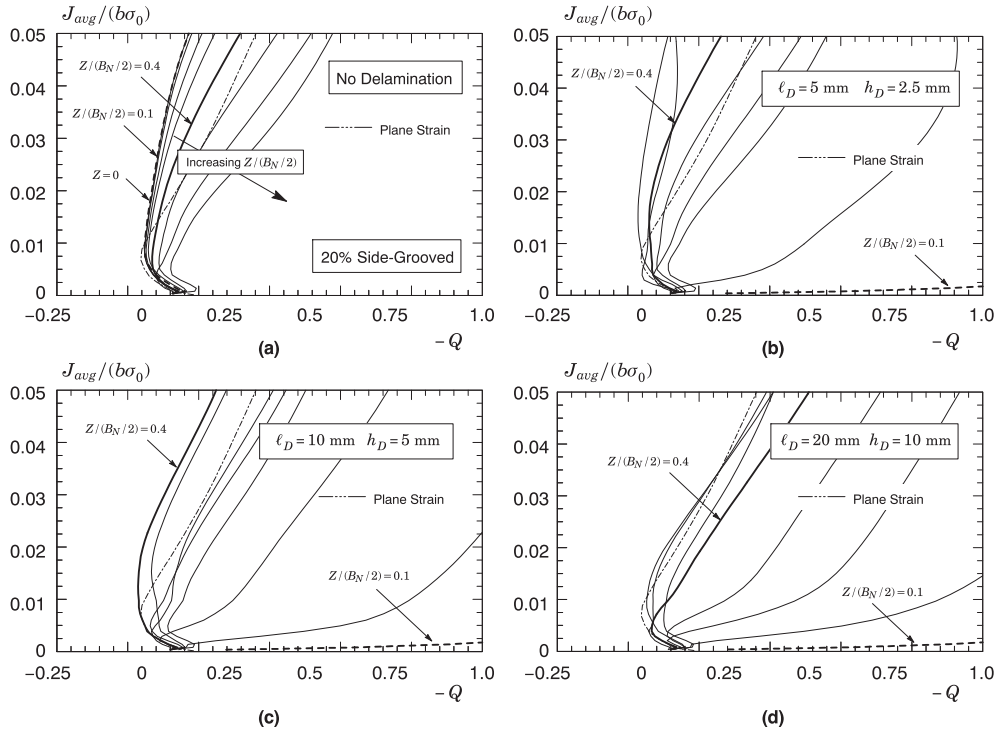

Fig. 11. J–Q trajectories at locations along the crack front for the C(T) model with 20% side-grooves: (a) No delamination; (b) 5 × 2.5 mm delamination; (c) 10 × 5 mm delamination; (d) 20 × 10 mm delamination.

the strong 3-D effects on J–Q trajectories in which the 3-D centerplane trajectories lie above the one for plane strain at all loading levels. This behavior can be understood by considering the character of Eq. (3) defining each J–Q curve. Since the scalar parameter Q derives from a two-dimensional viewpoint (thereby not considering its pointwise variation along the 3-D crack front), extensions and applications of Q within a fully 3-D framework to treat these crack front variations are not straightforward. For example, an alternative definition for Q, as suggested by Shih et al. [67], could be employed by building upon the notion of an average measure of constraint, Q_m, for a segment of the crack front, $s_a \le s \le s_b$, such that

$$Q_m = \frac{1}{s_a - s_b} \int_{s_a}^{s_b} Q(s) ds \tag{6}$$

which generalizes the overall constraint for 3-D cracked specimens by including the potentially strong variations of out-of-plane constraint over the crack front. However, since the primary interest of the present investigation is to assess the influence of a transverse delamination crack on crack front constraint (rather than comparing the fracture behavior for different specimen geometries), this option was not pursued. Moreover, these 3-D centerplane J–Q trajectories also reflect the global bending field which strongly impinges on the crack-tip fields for this geometry thereby resulting in a strong positive T-stress [48–50] for the C(T) configuration at the specimen centerplane [68]. Since a $Q = f(T)$ relation exists under SSY conditions [67], it becomes clear that positive T-stresses imply positive Q-values which are possibly higher than the Q-values corresponding to the plane-strain condition.

The J–Q trajectories for the C(T) models with varying delamination sizes are shown in Figs. 10(b–d) and 11(b-d). For all delamination sizes, the Q-values for the layer corresponding to $Z/(B/2) = 0.1$ ($Z/(B_N/2) = 0.1$) reveal a marked loss of constraint immediately upon loading (recall that this front location is very close to the prescribed delamination introduced into the model - see Section 4). As with the results shown in Figs. 6 and 7, the presence of a delamination crack gives rise to a pronounced stress redistribution over the specimen thickness thereby strongly affecting the levels of constraint over the crack front. To make our point, focus the attention on the J–Q trajectory at the crack front location $Z/(B/2) = 0.4$ ($Z/(B_N/2) = 0.4$) in the plots. This portion of the crack front maintains high levels of constraint (relative to other front locations), especially for moderate-to-large delamination crack sizes. What is particularly interesting, though, is that the evolution of Q with J for this crack front location (as well as nearby layers) displays little sensitivity to the delamination crack size for both the plane-sided and side-grooved models. These features suggest that, after a small transverse delamination crack forms at the specimen midplane, the near-tip stresses build-up rapidly at the center portion of the remaining thickness ligament ($Z/(B/2) \approx 0.4 \sim 0.5$ and $Z/(B_N/2) \approx 0.4 \sim 0.5$) until another transverse delamination crack possibly forms. Indeed, this is precisely the interpretation of the multiple delamination cracking observed in the fracture surface of the tested C(T) specimen shown in previous Fig. 2(a).

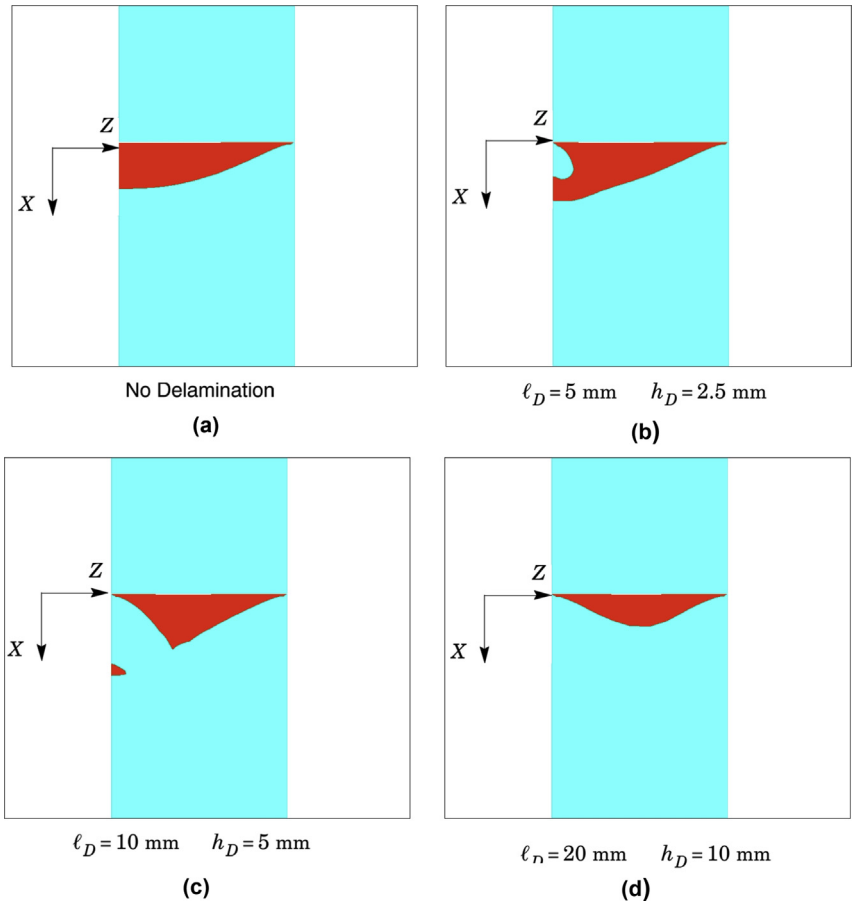

Fig. 12. Opening stress zones for which $\sigma_{yy} \ge 2\sigma_0$ over the crack front for the plane-sided C(T) models with and without transverse delamination crack at $J = 100$ kJ/m^2: (a) No delamination; (b) 5 × 2.5 mm delamination; (c) 10 × 5 mm delamination; (d) 20 × 10 mm delamination.

5.1.4. Crack front opening stress zones

Figs 12–15 show the opening stress contours for which $\sigma_{yy} \geq 2\sigma_0$ over the crack front for the 20% side-grooved C(T) model with and without a transverse delamination crack at two widely distinct levels of loading, $J = 100$ kJ/m^2 and $J = 500$ kJ/m^2. To the extent that the transverse delamination cracking process can be assumed as a stress-controlled fracture mechanism, the near-tip region associated with the spatial extent of the stress contour defined by $\sigma_{yy} \geq 2\sigma_0$ provides a quantitative measure of the fracture process zone of a few CTODs ahead of the macroscopic crack.

Consider first the opening stress zones for the plane-sided C(T) specimen displayed in Figs. 12 and 13. It is evident that the stress contours for the numerical models with and without a transverse delamination crack are markedly different and, further, that their spatial extent is sensitive to the delamination size. Here, the presence of a delamination crack clearly promotes a pronounced stress redistribution over the crack front for all load levels and delamination sizes. Observe, however, that the effects of delamination on the stress contour maps are less pronounced for the larger delamination cracks at all load levels. The high stress region $\sigma_{yy} \geq 2\sigma_0$ for the 20 × 10 mm delamination cracks is much less intense than the corresponding stress contour for the model without a transverse delamination. The trends shown here are consistent with those shown in previous Fig. 6 in that the introduction of a delamination crack produces a stress-free surface at the centerplane which relaxes the through-thickness constraint and shifts the near-tip highly stressed region to the middle portion of crack front.

Consider next the stress contour maps for the side-grooved C(T) geometry shown in Figs. 14 and 15. These results provide support to the following observations: (1) side-grooves promote a virtually uniform near-tip stress distribution over almost the entire net crack front; (2) side-grooves maintain high levels of near-tip stresses over a significant portion of the crack front at all load levels, particularly for the numerical models having a small-to-moderate delamination crack sizes (5 × 2.5 mm and 10 × 5mm delaminations) and (3) the side-grooved model with a larger delamination crack (20 × 10 mm) displays opening stress zones which are much less intense than the corresponding stress contour for other models. Again, as with the results shown in Sections 5.1.1 and 5.1.3, these trends are consistent with those shown previously in that the presence of a delamination crack relaxes the midplane stress, σ_{zz}, but with a relatively weak effect on the stress distribution over the remaining thickness ligament, particularly for small delamination crack sizes.

5.2. Delamination effects in clamped SE(T) specimens

The previous analyses demonstrate the rather strong influence of delamination cracking on 3-D crack front stresses and constraint in a deeply-cracked C(T) specimen with and without side-grooves. Those results clearly indicate that the formation of even a small transverse delamination crack at the specimen midplane promotes a pronounced stress redistribution over the specimen thickness which likely causes the formation of another transverse delamination crack at the center portion of the remaining thickness ligament. This section briefly examines whether these general features associated

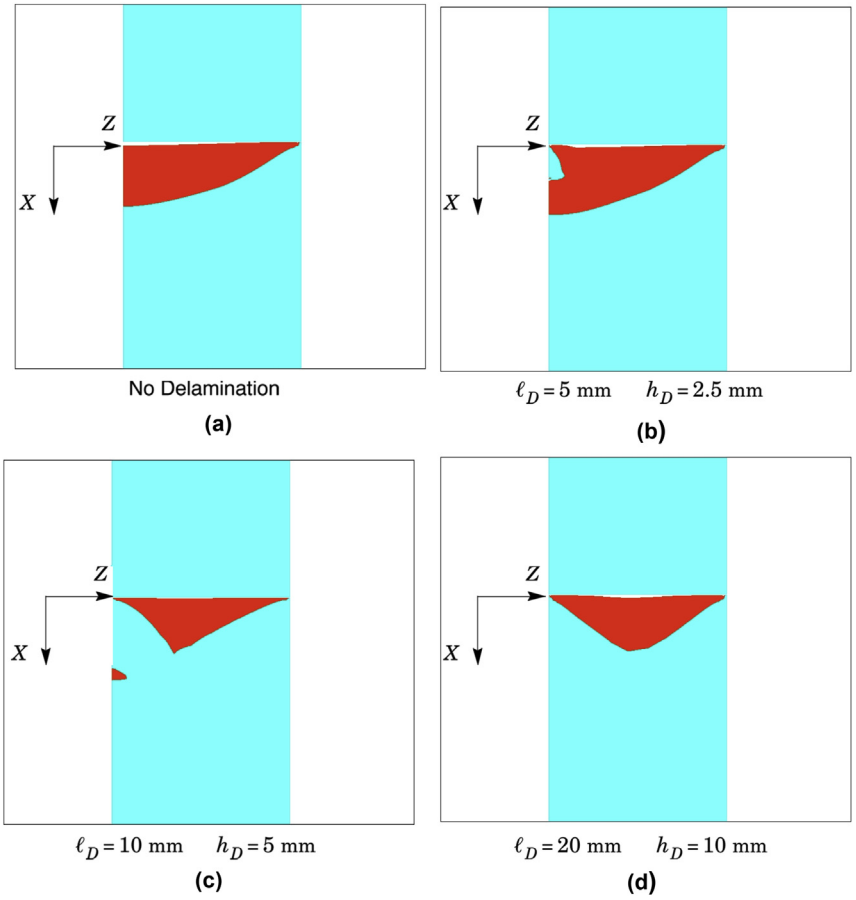

Fig. 13. Opening stress zones for which $\sigma_{yy} \geq 2\sigma_0$ over the crack front for the plane-sided C(T) models with and without transverse delamination crack at $J = 500$kJ/m^2: (a) No delamination; (b) 5 × 2.5 mm delamination; (c) 10 × 5 mm delamination; (d) 20 × 10 mm delamination.

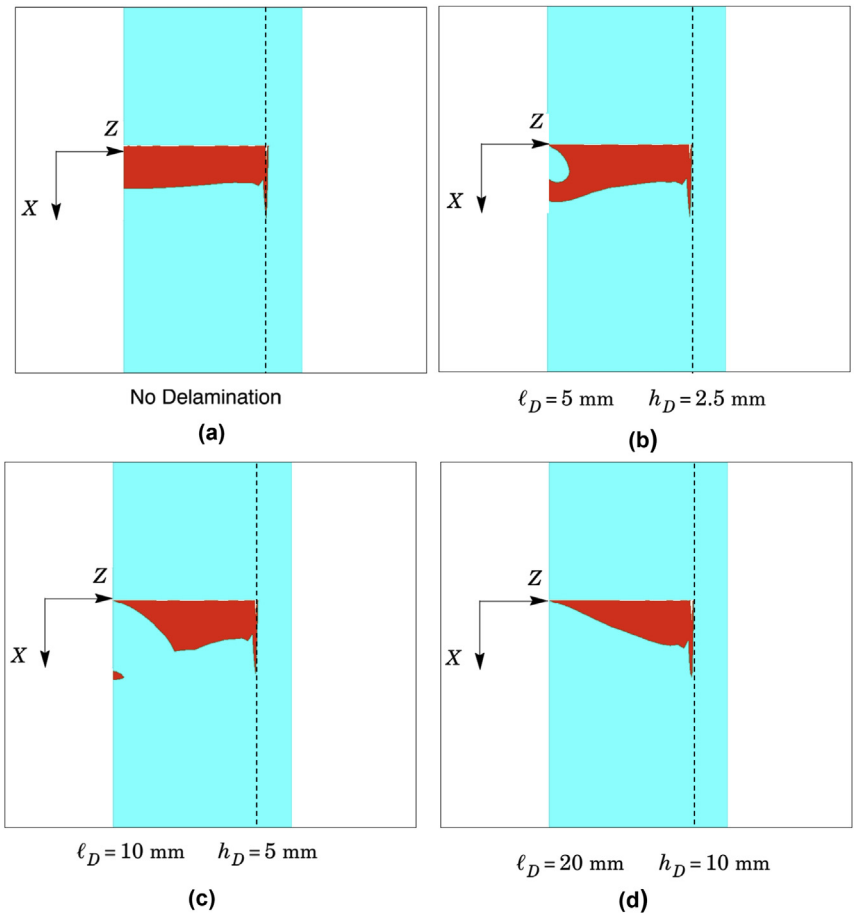

Fig. 14. Opening stress zones for which $\sigma_{yy} \geq 2\sigma_0$ over the crack front for the side-grooved C(T) models with and without transverse delamination crack at $J = 100$ kJ/m^2: (a) No delamination; (b) 5 × 2.5 mm delamination; (c) 10 × 5 mm delamination; (d) 20 × 10 mm delamination.

with delamination cracking effects on fracture behavior persist for low constraint specimen geometries. In particular, our interest here lies in the delamination cracking behavior for a clamped SE(T) specimen with crack size over specimen width ratio, $a/W = 0.4$, as this crack configuration is now extensively utilized to measure crack growth resistance properties for pipeline girth welds.

Figs. 16–18 provide key results to assess delamination effects in the analyzed SE(T) geometry. In these plots, the distribution of out-of-plane stresses, σ_{zz}, and local J-values over the crack front with increased load levels as well as the J–Q trajectories follow the same pattern as those corresponding to the side-grooved C(T) specimen shown previously. We present only the analysis for the model without delamination and with a delamination crack of 10 × 5 mm which are sufficiently descriptive of the delamination cracking behavior for this configuration. Results for the numerical models with other delamination crack sizes do not give additional insight so they are omitted in interest of space.

While the general features of delamination cracking effects in the clamped SE(T) configuration are qualitatively similar to those of C(T) specimens, there are some differences associated with the stress and constraint levels relative to the results displayed in Figs. 7, 9 and 11. As might be expected, this specimen geometry exhibits lower crack front constraint even at lower load levels as evidenced by the reduced out-of-plane stresses, σ_{zz}, and strong negative Q-values, which is fully consistent with tension dominated load states. For example, the σ_{zz}-stresses that develop along the crack front for the SE(T) geometry in Fig. 16 are lower by as much as 20 ~ 25% than those that develop in the side-grooved C(T) specimen shown in Fig. 7. Compare also the large differences in the J–Q trajectories for the SE(T) geometry shown in Fig. 18 with the corresponding curves for the side-grooved C(T) specimen displayed in Fig. 11. Here, despite the dramatic loss of constraint observed in the tension loaded configuration, the crack front location at $Z/(B_N/2) = 0.4$ also maintains higher levels of constraint (relative to other front locations in the specimen) after the introduction of a delamination crack. By contrast, the distribution of J_{local}/J_{avg} over the crack front for the side-grooved SE(T) and C(T) configurations are essentially similar (compare Figs. 17 and 9).

The above results may have important implications for the delamination cracking behavior in tension dominated load geometries, such as the analyzed clamped SE(T) specimen. Confining the present discussion to the development of delamination cracks by transgranular cleavage fracture of the weak planes (as already noted in Section 2), in which case the through-thickness near-tip stresses must satisfy a critical fracture stress criterion [20,40], it may never be possible to build up enough stress over the crack front leading to the formation of multiple transverse delamination cracks. Thus, even if a single delamination crack does form at the specimen centerplane, it may also plausibly be assumed that the through-thickness stresses will not recover to levels high enough to cause fracture of the weak planes located in the remaining thickness ligament.

6. Concluding remarks

This study describes an extensive numerical investigation of the crack front fields and effects of crack-tip constraint in conventional

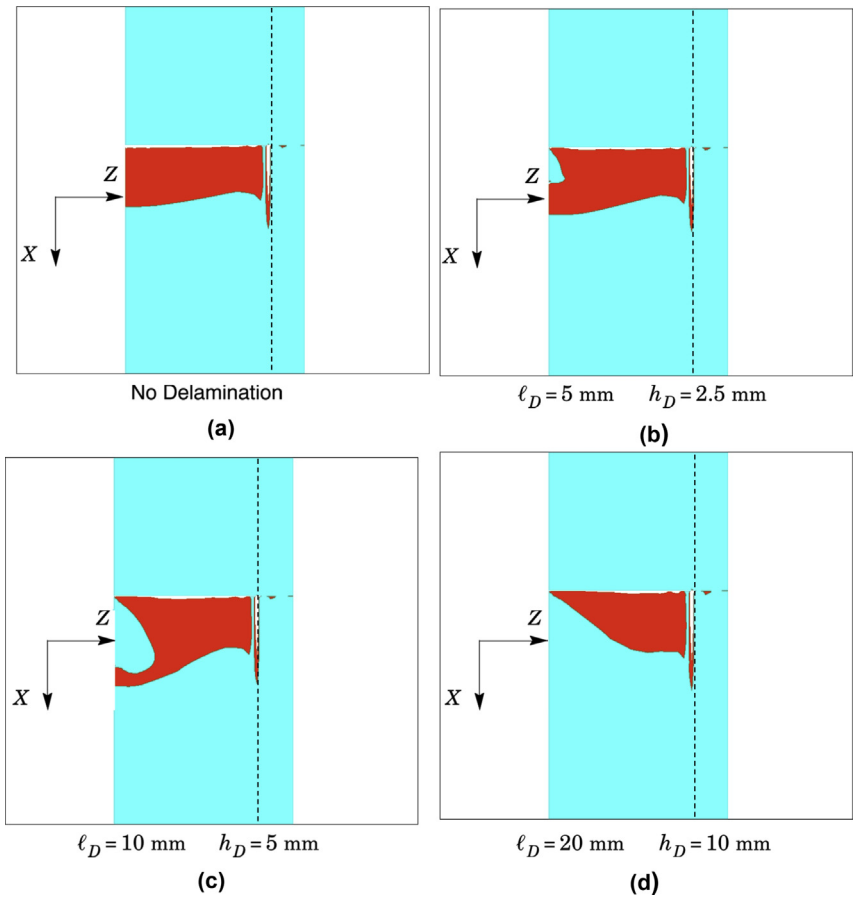

Fig. 15. Opening stress zones for which $\sigma_{yy} \geq 2\sigma_0$ over the crack front for the side-grooved C(T) models with and without transverse delamination crack at $J = 500$ kJ/m^2: (a) No delamination; (b) 5 × 2.5 mm delamination; (c) 10 × 5 mm delamination; (d) 20 × 10 mm delamination.

fracture specimens with prescribed crack-divider delamination cracks. The 3-D numerical models have a center-plane delamination crack with varying prescribed length, ℓ_D, and height, h_D, at the onset of loading which is adequately descriptive of the local conditions affecting macroscopic fracture behavior of the analyzed fracture specimens. The simulations are conducted on a plane-sided and side-grooved 1-T C(T) specimens and a clamped side-grooved SE(T) geometry having mechanical properties corresponding to a controll-rolled API X70 pipeline grade steel tested at room temperature to measure the crack growth resistance properties. This class of material is strongly susceptible to development of transverse delamination cracking (splits) along the rolling direction as a result of its marked anisotropy in microstructural and metallurgical features. Fracture toughness testing of this steel also provided an experimental basis to choose the range of delamination sizes adopted in this investigation defined by $\ell_D \times h_D = 5 \times 2.5$, 10×5 and 20×10 mm. The work described here supports the following conclusions:

1. Formation of a transverse center-plane delamination crack creates a stress-free surface at the centerplane thereby relaxing the through-thickness constraint and, at the same time, shifting the near-tip highly stressed region to the middle portion of the remaining specimen thickness ligament corresponding approximately to crack front locations of $Z/(B/2) \approx 0.4 \sim 0.5$ ($Z/(B_N/2) \approx 0.4 \sim 0.5$). Perhaps more importantly, the formation of a crack divider delamination at the specimen centerplane drastically changes the distribution of the macroscopic driving force over the crack front with potential significant effects on the measured fracture toughness. In particular, the onset of through-thickness splitting effectively divides the bulk of the specimen so that only a reduced portion of the crack front is subjected to high levels of crack-tip loading (as measured by J) thereby potentially enhancing fracture toughness.
2. The 3-D numerical analyses show that the formation of even a small transverse delamination crack at the specimen midplane promotes a pronounced stress redistribution over the specimen thickness which likely causes the formation of another transverse delamination crack at the center portion of the remaining thickness ligament. Since the range of delamination sizes adopted in this investigation is perhaps less than desirable to fully assess the effects of transverse delamination cracking, it is somewhat difficult to draw definitive conclusions on a “critical” delamination size from which changes in the specimen fracture behavior become important. Nevertheless, the present results clearly indicate the strong effects of small crack divider delaminations at the specimen centerplane on the crack front stresses with potential to increase fracture toughness measured in fracture tests. Moreover, while the present analyses do not incorporate the growth of the delamination crack with increased loading, and thus not including history effects on the evolving crack front stress fields and crack front constraint, the results provide very plausible qualitative support for the multiple delamination cracking observed in the fracture surface of the tested C(T) specimen.

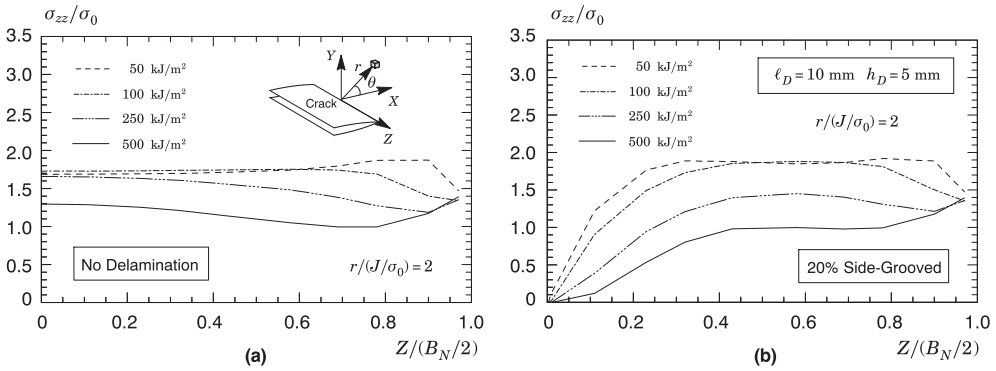

Fig. 16. Distribution of out-of-plane stresses (σ_{zz}) over the crack front with increased load levels at the normalized crack-tip distance, $r/(J/\sigma_0) = 2$ for the clamped SE(T) model with 20% side-grooves: (a) No delamination; (b) 10 × 5 mm delamination.

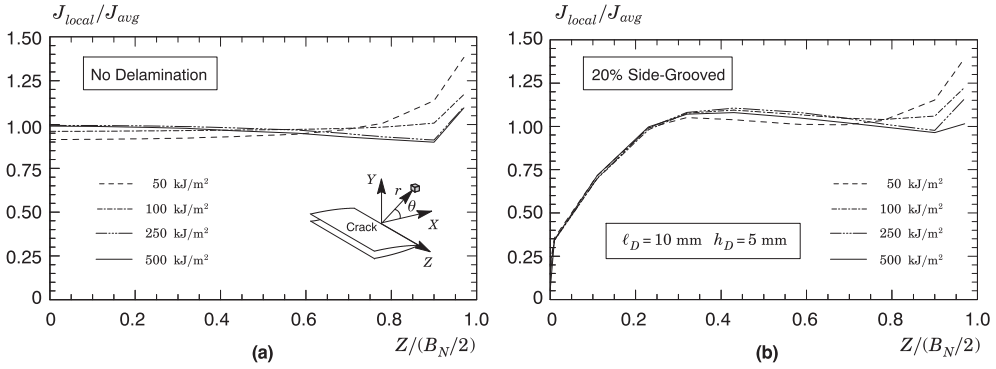

Fig. 17. Distribution of the *J*-integral over the crack front with increased deformation levels for the clamped SE(T) model with 20% side-grooves: (a) No delamination; (b) 10 × 5 mm delamination.

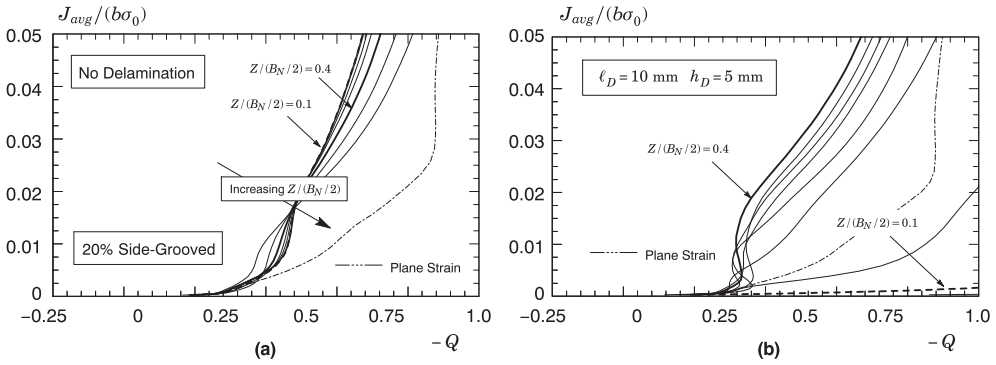

Fig. 18. *J*–*Q* trajectories at locations along the crack front for the clamped SE(T) model with 20% side-grooves: (a) No delamination; (b) 10 × 5 mm delamination.

3. Introduction of side-grooves in the fracture specimens does not change significantly the gross features and general trends associated with delamination cracking effects on macroscopic fracture behavior. However, the presence of side-grooves does maintain high levels of crack front constraint over a much larger portion of the specimen thickness. Thus, it appears that side-grooves may actually mitigate the effects of delamination cracking on the stress redistribution over the crack front, particularly for small delamination crack sizes.
4. The numerical results also show that the general features of delamination cracking effects in the clamped SE(T) configuration are qualitatively similar to those of C(T) specimens. However, the near-tip stresses that develop along the crack front for this geometry are markedly lower than the corresponding stresses in the side-grooved C(T) specimen. Thus, even if a single delamination crack forms at the specimen centerplane, the through-thickness stresses may not recover to levels high enough to cause a secondary fracture (split) of the remaining thickness ligament.

It is also of interest to note that though the onset of a transverse center-plane delamination crack relaxes crack front constraint and potentially enhances the fracture toughness that would be measured in fracture tests of standard specimens, the beneficial increased measured toughness values are observed only for fracture in *L*–*T* or *T*–*L* direction associated with a mechanism of

crack-divider delamination toughening in a wide class of structural alloys, including pipeline grade steels. However, improvements in measured fracture toughness due to delamination effects are plausibly not typical of *all* structural materials due to the potential concurrence of splitting and other micromechanisms which are detrimental to the fracture resistance. For example, Pyshmintsev et al. [13] have recently showed that the occurrence of multiple transverse delamination cracks in single-edge notched tensile specimens extracted from an API X80 plate actually promotes a decrease in the specific energy measured at ductile fracture, which is strongly related to a plastic collapse mechanism of the remaining thickness ligament in their work. Nevertheless, the present investigation, when taken together with previous studies, provides compelling evidence for the toughening mechanism of a crack-divider delamination. Ongoing investigation also focuses on assessing delamination effects in the fracture behavior of subsized SE(B) specimens made of nanostructured ferritic alloys (NFA) for nuclear fusion power reactors and will be presented in a forthcoming publication.

Acknowledgments

This investigation is supported by Fundação de Amparo à Pesquisa do Estado de São Paulo (FAPESP) through Grant 2012/13053-2 and by the Brazilian Council for Scientific and Technological Development (CNPq) through Grants 473975/2012-2 and 306193/2013-2. This work was partly conducted while the first author (CR) was on sabbatical at the University of California at Santa Barbara (UCSB). The authors also acknowledge the many useful discussions and contributions of their colleague Prof. George R. Odette (UCSB).

References

[1] Bai Y. Pipelines and risers. Elsevier; 2001.
[2] Bai Y, Bai Q. Subsea pipelines and risers. Elsevier; 2005.
[3] Palmer AC, King RA. Subsea pipeline engineering. 2nd ed. PennWell Corporation; 2008.
[4] Langhelle MB. Pipelines for development at deep water fields [Master's thesis], Faculty of Science and Technology. University of Stavanger; 2011.
[5] Tanaka T. Controlled rolling of steel plate and strip. Int Met Rev 1981;4:185–212.
[6] Sha W. Steels: from materials science to structural engineering. Springer; 2013.
[7] Fearnehough GD. Fracture propagation control in gas pipelines: a survey of relevant studies. Int J Press Vessel Pip 1974;2:257–82.
[8] Joo MS, Suh DW, Bhadeshia HKDH. Mechanical anisotropy in steels for pipelines. ISIJ Int 2013;53:1305–14.
[9] Canadian Standard Association. Oil & gas pipeline systems. 2007. CSA Z662.
[10] Veritas Det Norske. Submarine pipeline systems. Offshore Standard; 2013. OS-F101.
[11] Kiefner JF, Eiber RJ. Failure of pipelines. In: Becker WT, Shipley RJ, editors. ASM Handbook, Vol. 11. Materials Park, OH: ASM International; 2002. p. 2791–818.
[12] Olalla VC, Gervasyev A, Pyshmintsev I, Sanchez N, Thibaux P, Petrov RH, et al. Microstructural control of ductile crack arrestability in hsla pipeline steels. In: 6th international pipeline technology conference (PTC 2013), Ostend, Belgium; 2013.
[13] Pyshmintsev I, Gervasyev A, Olalla VC, Petrov R, Arabey A. Mechanical and metallurgical aspecas of the resistance to ductile fracture propagation in the new generation of gas pipelines. In: 10th international pipeline conference (IPC 2006), Calgary, Canada; 2014.
[14] Transportation Safety Board of Canada. Natural gas pipeline rupture. 1994. Tech. Rep. P94H0003, Canada.
[15] ASM International. ASM handbook. Corrosion, Vol. 13. Materials Park, OH: ASM International; 2002.
[16] ASM International. ASM handbook. Fatigue and fracture, Vol. 19. Materials Park, OH: ASM International; 1996.
[17] Rao KTV, Yu W, Ritchie RO. Cryogenic toughness of commercial aluminum-lithium alloys: role of delamination toughness. Metall Trans A 1989;20A:485–97.
[18] Morrison WB. Influence of testing direction on the mechanical properties of wrought steel. Met Technol 1975;2:33–41.
[19] Bramfitt BL, Marder AR. A study of the delamination behavior of a very low-carbon steel. Metallurgical Mater Trans A 1977;8A:1263–73.
[20] Baldi G, Buzzichelli G. Critical stress for delamination fracture in HSLA steels. Metal Sci 1978:459–72.
[21] Song R, Ponge D, Raabe D. Mechanical properties of an ultrafine grained C-Mn steel processed by warm deformation and annealing. Acta Mater 2005;53:4881–92.
[22] Song R, Ponge D, Raabe D, Speer JG, Matlock DK. Overview of processing, microstructure and mechanical properties of ultrafine grained BCC steels. Mater Sci Eng A 2006;441:1–17.
[23] Inoue T, Yin F, Kimura Y, Tsuzaki K, Ochiai S. Delamination effect on impact properties of ultrafine-grained low-carbon steel processed by warm caliber rolling. Metall Trans A 2010;41A:341–55.
[24] Yan W, Sha W, Zhu L, Wang W, Shan Y-Y, Yang K. Delamination fracture related to tempering in a high-strength low-alloy steel. Metall Trans A 2010;41A:159–71.
[25] Guo W, Dong H, Lu M, Zhao X. The coupled effects of thickness and delamination on cracking resistance of X70 pipeline steel. Int J Press Vessels Pip 2002;79:403–12.
[26] Shin SY, Woo KJ, Hwang B, Kim S, Lee S. Fracture toughness analysis in transition temperature region of three American Petroleum Institute X70 and X80 pipeline steels. Metallurgical Mater Trans A 2009;40A:867–76.
[27] Shin SY, Hong S, Bae J-H, Kim K, Lee S. Separation phenomenon occurring during the Charpy impact test of API X80 pipeline steels. Metallurgical Mater Trans A 2009;40A:2333–49.
[28] Hong S, Shih YS, Lee S, Kim NJ. Effects of specimen thickness and notch shape on fracture modes in the drop weight tear test of api x70 and x80 linepipe steels. Metallurgical Mater Trans A 2011;42A:2619–32.
[29] Rao KTV, Ritchie RO. Mechanical properties of AI-Li alloys - Part 1: fracture toughness and microstructure. Mater Sci Technol 1989;5:882–95.
[30] Rao KTV, Ritchie RO. Mechanical properties of AI-Li alloys - Part 2: fatigue crack propagation. Mater Sci Technol 1989;5:896–907.
[31] Pilhagen J, Sandström R. Loss of constraint during fracture toughness testing of duplex stainless steels. Eng Fract Mech 2013;99:239–50.
[32] Kalyanam S, Beaudoin AJ, Dodds RH, Barlat F. Delamination cracking in advanced aluminum-lithium alloys - experimental and computational studies. Eng Fract Mech 2009;76:2174–91.
[33] Hippert E. Experimental investigation of ductile fracture behavior in API X70 grade pipeline steels and applicability of crack growth resistance curves to predict the burst pressure in longitudinally cracked pipes [Ph.D. thesis]. Polytechnic School, University of São Paulo; 2001 (In Portuguese).
[34] Joyce JA. Manual on elastic-plastic fracture: laboratory test procedure. ASTM Manual Series MNL 27. ASTM International; 1996.
[35] Anderson TL. Fracture mechanics: fundaments and applications. 3rd ed. Boca Raton, FL: CRC Press; 2005.
[36] American Society for Testing and Materials. Standard test method for measurement of fracture toughness. ASTM E1820–2011. 2011.
[37] Hippert E, Ruggieri C. Experimental and numerical investigation of ductile crack extension in a high strength pipeline steel. In: ASME 2001 pressure vessels & piping conference (PVP 2001), Atlanta, GA; 2001.
[38] American Society for Testing and Materials. Standard test methods for tension testing of metallic materials. ASTM E8–11. 2011.
[39] Silva MC, Hippert E, Ruggieri C. Experimental investigation of ductile tearing properties for an API X70 and X80 pipeline steel. In: ASME 2005 pressure vessels & piping conference (PVP 2005), Denver, CO; 2005.
[40] Zok F, Embury JD. On the analysis of delamination fractures in high-strength steels. Metall Trans A 1990;21A:2565–75.
[41] Dodds RH, Shih C, Anderson T. Continuum and micro-mechanics treatment of constraint in fracture. Int J Fract 1993;64:101–33.
[42] Nevalainen M, Dodds RH. Numerical investigation of 3-D constraint effects on brittle fracture in SE(B) and C(T) specimens. Int J Fract 1995;74:131–61.
[43] Rice JR. A path independent integral and the approximate analysis of strain concentration by notches and cracks. J Appl Mech 1968;35:379–86.
[44] O'Dowd N, Shih C. Family of crack-tip fields characterized by a triaxiality parameter: part I - structure of fields. J Mech Phys Solids 1991;39:989–1015.
[45] O'Dowd N, Shih C. Family of crack-tip fields characterized by a triaxiality parameter: part II - fracture applications. J Mech Phys Solids 1992;40:939–63.
[46] Rice JR. Mechanics of crack tip deformation and extension by fatigue. In: Grosskreutz J, editor. fatigue crack propagation. ASTM STP 415. Philadelphia: American Society for Testing and Materials; 1967. p. 247–311.
[47] Larsson SG, Carlsson AJ. Influence of non-singular stress terms and specimen geometry on small scale yielding at crack-tips in elastic-plastic materials. J Mech Phys Solids 1973;21:447–73.
[48] Betegon C, Hancock JW. Two-parameter characterization of elastic-plastic crack tip fields. J Appl Mech 1991;58:104–13.
[49] Du ZZ, Hancock JW. The effect of non-singular stresses on crack-tip constraint. J Mech Phys Solids 1991;39:555–67.
[50] Parks DM. Advances in characterization of elastic-plastic crack-tip fields. In: Argon AS, editor. Topics in fracture and fatigue. Springer Verlag; 1992. p. 59–98.
[51] Dodds R, Anderson T, Kirk M. A framework to correlate a/W ratio effects on elastic-plastic fracture toughness (J_c). Int J Fract 1991;48:1–22.
[52] Cravero S, Ruggieri C. Correlation of fracture behavior in high pressure pipelines with axial flaws using constraint designed test specimens - part I: plane-strain analyses. Eng Fract Mech 2005;72:1344–60.
[53] Det Norske Veritas. Fracture control for pipeline installation methods introducing cyclic plastic strain. DNV-RP-F108. 2006.

[54] Mathias LLS, Sarzosa DFB, Ruggieri C. Effects of specimen geometry and loading mode on crack growth resistance curves of a high-strength pipeline girth weld. Int J Press Vessel Pip 2013;111–112:106–19.
[55] Sarzosa DFB, Ruggieri C. A numerical investigation of constraint effects in circumferentially cracked pipes and fracture specimens including ductile tearing. Int J Press Vessel Pip 2014;120–121:1–18.
[56] Dowling NE. Mechanical behavior of materials: engineering methods for deformation, fracture and fatigue. 2nd ed. New Jersey: Prentice Hall; 1999.
[57] Dodds RH, Ruggieri C, Koppenhoefer K. 3-d effects on models for transferability of cleavage fracture toughness. In: Underwood JH, MacDonald BD, Mitchell MR, editors. Fatigue and fracture mechanics. ASTM STP 1321, Vol. 28. Philadelphia: American Society for Testing and Materials; 1997. p. 179–97.
[58] Shih CF. Relationship between the *J*-integral and the crack opening displacement for stationary and extending cracks. J Mech Phys Solids 1981;29:305–26.
[59] Healy B, Gullerud A, Koppenhoefer K, Roy A, RoyChowdhury S, Petti J, et al. WARP3D: 3-D nonlinear finite element analysis of solids for fracture and fatigue processes. Tech. rep. Urbana-Champaign,: University of Illinois; 2014., http://code.google.com/p/warp3d.
[60] Moran B, Shih CF. A general treatment of crack tip contour integrals. Int J Fract 1987;35:295–310.
[61] Al-Ani AM, Hancock JW. *J*-dominance of short cracks in tension and bending. J Mech Phys Solids 1991;39:23–43.
[62] Williams ML. On the stress distribution at the base of a stationary crack. J Appl Mech 1957;24:109–14.
[63] Ruggieri C. FRACTUS2D: numerical computation of fracture mechanics parameters for 2-D cracked solids. Tech. rep. University of Sao Paulo; 2011.
[64] McMeeking RM, Parks DM. On criteria for *J*-dominance of crack-tip fields in large-scale yielding. In: Landes JD, Begley JA, Clarke GA, editors. Elastic-plastic fracture. ASTM STP 668. Philadelphia: American Society for Testing and Materials; 1979. p. 175–94.
[65] Trovato E, Ruggieri C. Micromechanics characterization of constraint and ductile tearing effects in small scale yielding fracture. Int J Solids Struct 2001;38:2171–87.
[66] Silva LAL, Cravero S, Ruggieri C. Correlation of fracture behavior in high pressure pipelines with axial flaws using constraint designed test specimens - part II: 3-D effects on constraint. Eng Fract Mech 2006;76:2123–38.
[67] Shih C, O'Dowd N, Kirk MT. A framework for quantifying crack tip constraint. In: Hackett EM, Schwalbe K-H, Dodds RH, editors. Constraint effects in fracture. ASTM STP 1171. Philadelphia: American Society for Testing and Materials; 1993. p. 2–20.
[68] Sherry AH, France CC, Goldthorpe MR. Compendium of *T*-stress solutions for two and three dimensional cracked geometries. Fatigue Fract Eng Mater Struct 1995;18(1):141–55.